Optics Letters

Dual-view photoacoustic microscopy for quantitative cell nuclear imaging

De Cai,[1,2,†] Terence T. W. Wong,[1,3,†] Liren Zhu,[1] Junhui Shi,[1] Sung-Liang Chen,[2] and Lihong V. Wang[1,*]

[1]Caltech Optical Imaging Laboratory, Andrew and Peggy Cherng Department of Medical Engineering, Department of Electrical Engineering, California Institute of Technology, Pasadena, California 91125, USA
[2]University of Michigan-Shanghai Jiao Tong University Joint Institute, Shanghai Jiao Tong University, Shanghai 200240, China
[3]Currently at Translational and Advanced Bioimaging Laboratory, Department of Chemical and Biological Engineering, Hong Kong University of Science and Technology, Hong Kong, China
*Corresponding author: LVW@Caltech.edu

Received 25 July 2018; accepted 31 August 2018; posted 10 September 2018 (Doc. ID 340705); published 3 October 2018

Optical-resolution photoacoustic microscopy (OR-PAM) is an emerging imaging modality for studying biological tissues. However, in conventional single-view OR-PAM, the lateral and axial resolutions—determined optically and acoustically, respectively—are highly anisotropic. In this Letter, we introduce dual-view OR-PAM to improve axial resolution, achieving three-dimensional (3D) resolution isotropy. We first use 0.5 μm polystyrene beads and carbon fibers to validate the resolution isotropy improvement. Imaging of mouse brain slices further demonstrates the improved resolution isotropy, revealing the 3D structure of cell nuclei in detail, which facilitates quantitative cell nuclear analysis.

OCIS codes: (110.0180) Microscopy; (110.5120) Photoacoustic imaging; (170.3880) Medical and biological imaging; (100.6890) Three-dimensional image processing.

https://doi.org/10.1364/OL.43.004875

Optical-resolution photoacoustic microscopy (OR-PAM) has found broad applications in imaging biological objects ranging from organelles to organs [1,2]. OR-PAM can achieve lateral resolution in several micrometers or even sub-micrometers [3,4] by tightly focusing the optical focal spot. However, axial resolution in OR-PAM, which is determined by the bandwidth of an ultrasonic transducer matching the targeted tissue penetration, is typically limited to tens of micrometers. Anisotropic resolutions hinder OR-PAM from revealing accurate three-dimensional (3D) structures of biological tissue.

OR-PAM with ultraviolet laser illumination has recently been exploited to image human breast and mouse brain tissues with specific cell nuclear contrast for cancer diagnosis and intraoperative margin assessment as well as for basic research in neuroscience [5–8]. The resolution anisotropy in OR-PAM with ultraviolet laser illumination is particularly severe due to finer optical lateral resolution enabled by shorter laser wavelength (e.g., 0.33 μm lateral resolution versus 48 μm axial resolution [5]).

In recent years, different approaches have been developed to enhance axial resolution, thus improving the resolution isotropy of OR-PAM. Wide bandwidth ultrasonic transducers [9] and optical ultrasonic detectors [10] have been utilized for high-frequency ultrasonic detection to refine axial resolution, yet the severe attenuation of high-frequency acoustic waves in biological tissue limits imaging depth and working distance. Although the Weiner deconvolution algorithm has also been utilized to improve axial resolution, improvement is not significant due to the stringent signal-to-noise ratio (SNR) requirement [11]. Moreover, optical sectioning has been achieved in OR-PAM by nonlinear effects such as two-photon absorption [12] and Grüneisen relaxation [13,14]; the imaging speed, however, is reduced owing to the need for additional depth scanning. Multi-view optical illumination has been applied in both light sheet fluorescence microscopy [15,16] and OR-PAM [17,18], to improve resolution isotropy. In particular, in a previous demonstration of multi-view OR-PAM [17], the sample was required to be rotated to achieve multi-view optical illumination, which may introduce undesirable movement of the sample. Furthermore, previous work [17,19] proved that dual-view is sufficient in providing isotropic resolution on the condition that a complementary, perpendicular view is acquired and properly merged.

In this Letter, we report dual-view OR-PAM (DV-OR-PAM) with ultraviolet laser illumination, developed to improve resolution isotropy. The schematic of DV-OR-PAM is illustrated in Fig. 1. The 5 mm diameter UV laser beam (Wedge-HF-266, 266 nm wavelength, Bright Solutions SRL) is split into two orthogonal beams, named as left and right view laser beams hereafter. The two beams are then focused onto the sample from below, each by an aspheric lens with a numerical aperture of 0.29 (AFL25-40-S-U, asphericon GmbH). The ultrasonic waves generated inside the sample through the photoacoustic effect are detected by an ultrasonic transducer (V358-SU, 50-MHz central frequency, 88% bandwidth

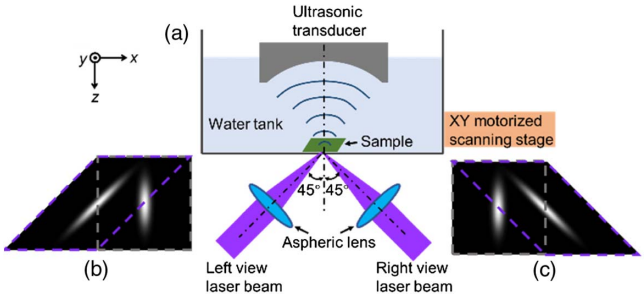

Fig. 1. (a) Schematic of the DV-OR-PAM system. (b), (c) Shear transformed images in purple dashed boxes for left and right views, respectively. The corresponding original images are enclosed in gray dashed boxes for comparison.

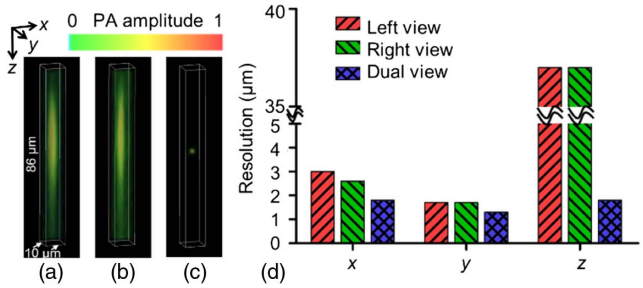

Fig. 2. Resolution calibration for DV-OR-PAM using 0.5 μm diameter beads as point objects. Volumetrically rendered bead images for (a) left view, (b) right view, and (c) dual view, respectively. (d) Resolutions in the x, y, and z directions for left view, right view, and dual view images.

(one-way), Olympus NDT, Inc.) with a homemade concave lens at the front to provide acoustic focusing. After electrical amplification (56 dB, two ZFL-500LN+, Mini-Circuits, Inc.), the signal is digitized by a data acquisition card (ATS9350, Alazar Technologies, Inc.) at a sampling rate of 500 MS/s and sent to a computer for afterward processing. Each A-line signal is converted to a depth-resolved profile by taking the envelope. The water tank with the sample is raster scanned with a step size of 0.31 μm on the x–y plane by a motorized scanning stage (PLS-85, PI miCos GmbH) to obtain a single-view 3D image (e.g., left view). The sample is then re-scanned with the same configuration but with the right view laser beam to obtain an orthogonal-view 3D image.

The axial pixel size in the original 3D images is 3 μm (assuming the speed of sound is 1.5 mm/μs), which is larger than the lateral pixel size (0.31 μm). Interpolation is applied in the axial direction to make the pixel size isotropic. The optical axes of the dual-view beams, together with the detection axis of the ultrasonic transducer, are coplanar on the x–z plane and symmetrically aligned with respect to the ultrasonic transducer axis, both with 45 deg tilt angles. Left and right view images are transformed to a coordinate system of the sample for image registration through an affine transformation, including both shear and translation transformations, as shown in Eq. (1), where x', y', and z' are the coordinates in the sample system; x, y, and z are the local coordinates for the two views; t_x, t_y, and t_z constitute the translation vector for the transformation matrix. Shear transformation is performed on the x–z plane. The x coordinate transformations for left and right view images are $x' = x - z$ and $x' = x + z$, respectively. The effect of shear transformation is illustrated in Figs. 1(b) and 1(c) for left and right view images, respectively:

$$\begin{bmatrix} x' \\ y' \\ z' \\ 1 \end{bmatrix} = \begin{bmatrix} 1 & 0 & \pm 1 & t_x \\ 0 & 1 & 0 & t_y \\ 0 & 0 & 1 & t_z \\ 0 & 0 & 0 & 1 \end{bmatrix} \begin{bmatrix} x \\ y \\ z \\ 1 \end{bmatrix}. \quad (1)$$

Sub-resolution polystyrene beads with a 0.5 μm average diameter, together with a target to be imaged, were embedded in agarose gel as registration markers [20]. The beads were detected in the two view images and localized as point objects for registration. Values of t_x, t_y, and t_z in Eq. (1) are optimized by globally minimizing the total displacement between the corresponding registration point objects between left and right view images.

The sub-resolution beads were also used to extract the point spread functions (PSFs) in the two view images. Single-bead images were averaged over four acquisitions and normalized to serve as PSFs of the two view images. The PSFs were also affine transformed accordingly to co-register. The co-registered two view images and PSFs were then used for dual-view Richardson–Lucy deconvolution with 10 iterations [16,20] to obtain a single dual-view image.

We used the sub-resolution beads to calibrate resolutions of the original two images and the dual-view image. The volumetrically rendered 3D images of a single bead are shown in Figs. 2(a)–2(c) for the left view, right view, and dual view, respectively. Note that the original left and right view images were not affine transformed. The resolutions defined by the full width at half maximum are plotted in Fig. 2(d). Resolutions on the x axis are 3.0 μm, 2.6 μm, and 1.8 μm for the left view, right view, and dual view, respectively. Resolutions on the y axis are 1.7 μm, 1.7 μm, and 1.3 μm for the left view, right view, and dual view, respectively. The acoustically determined axial resolution of the original left and right view images, far worse than the optically defined lateral resolutions, is 37 μm, which accounts for the elongated bead profiles and resolution anisotropy [Figs. 2(a) and 2(b)]. Dual-view imaging greatly improved axial resolution to 1.8 μm (i.e., by a factor of 20), making the bead profile nearly isotropic in 3D [blue bars in Fig. 2(d)]. As the dual-view deconvolution is performed on the x–z plane, the x–z resolution isotropy—quantified as the ratio between the x and z resolutions—is improved from 12.3/14.2 (left view/right view) to 1.0. Resolutions in the original two views in the x direction are about $\sqrt{2}$ larger than the resolutions in the y direction because of the oblique 45 deg illumination with respect to the z axis. Resolution on the y axis for oblique illumination is the same as normal incident illumination. In addition, x and y resolutions are improved in the dual-view images due to deconvolution in the reconstruction algorithm.

To better demonstrate the performance of DV-OR-PAM, we made a 3D tissue phantom composed of 6 μm diameter carbon fibers placed at different depths and orientations. 3D images of the carbon fibers are shown in Figs. 3(a)–3(c) for the left view, right view, and dual view, respectively. A clearer carbon fiber network is revealed in the dual-view

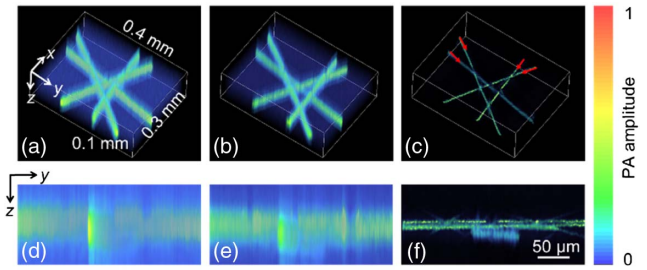

Fig. 3. Imaging of four 6 μm diameter carbon fibers (indicated by red arrows) with different depths and orientations. Volumetric carbon fiber images for (a) left view, (b) right view, and (c) dual view. *y*–*z* MAP images to show the depth information for (d) left view, (e) right view, and (f) dual view.

image due to enhanced axial resolution and ∼9 dB SNR improvement. The improved resolution isotropy in DV-OR-PAM can reveal finer depth information, as shown in Figs. 3(d)–3(f), which are the *y*–*z* maximum amplitude projections (MAPs) of the volumetric images shown in Figs. 3(a)–3(c). The carbon fibers at different depths are clearly revealed in the dual-view *y*–*z* MAP image, while in the original two *y*–*z* MAP images, the two carbon fibers are unresolved due to poor axial resolution.

We imaged mouse brain slices of 200 μm thickness [6] to further validate DV-OR-PAM. To enlarge the imaging area, the step size was set as 0.62 μm with an imaging field of view over 1 mm × 0.5 mm along the *x* and *y* axes. The absorption contrast at the 266 nm wavelength in mouse brains is predominantly cell nuclei [8], which appear to be the brightest features in the images. The *x*–*y* MAP images of the mouse brain slice are shown in Figs. 4(a)–4(c) for the left view, right view, and dual view, respectively. To better visualize the improved image quality of DV-OR-PAM, zoomed-in images of the red dashed boxes are shown in Figs. 4(d)–4(f). The cell nuclei can be better identified in the dual-view image with improvement in both resolution and SNR (by ∼10 dB). Specifically, the cell nuclear profile in the blue dashed boxes, which cannot be resolved in the original two images [Figs. 4(g) and 4(h)], can be clearly revealed in the dual-view image, as shown in Fig. 4(i). The detailed internal structure of the cell nuclei provided by DV-OR-PAM can potentially facilitate accurate cancer diagnosis [21,22].

We have digitally extracted the image stacks on the *x*–*y* plane of the red dashed regions at five different depths with an interval of 3.1 μm. The image stacks are shown in Figs. 4(j)–4(l) for the left view, right view, and dual view images, respectively. In the original images, the image stacks at five different depths show a similar brightness because of poor axial resolution, while in the dual-view image, different layers of cell nuclei are clearly demonstrated.

With the improved axial resolution, it is possible to reveal the accurate 3D shape of a cell nucleus, as shown in Figs. 5(a)–5(c), corresponding to the red dashed regions shown in Figs. 4(a)–4(c). We quantitatively analyzed the cell nuclear volume, with a histogram plotted in Fig. 5(d). The average cell nuclear volumes are 5312 ± 2202 μm^3 and 6665 ± 2253 μm^3 for left and right views, respectively. While in the dual-view image, the average cell nuclear volume is 778 ± 396 μm^3, which is much

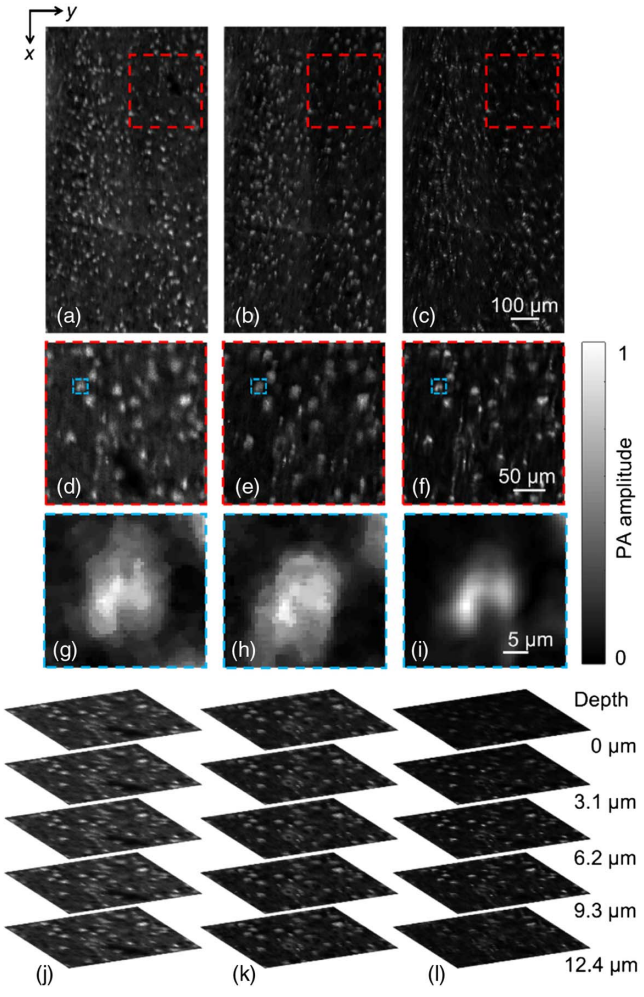

Fig. 4. Imaging of a mouse brain slice. *x*–*y* MAP images for (a) left view, (b) right view, and (c) dual view, respectively. (d)–(f) Zoomed-in red dashed regions of (a)–(c). (g)–(i) Zoomed-in blue dashed regions of (d)–(f), showing the cell nuclear profile. Digitally reconstructed *x*–*y* images of the red dashed regions at five different depths with an interval of 3.1 μm for (j) left view, (k) right view, and (l) dual view, respectively.

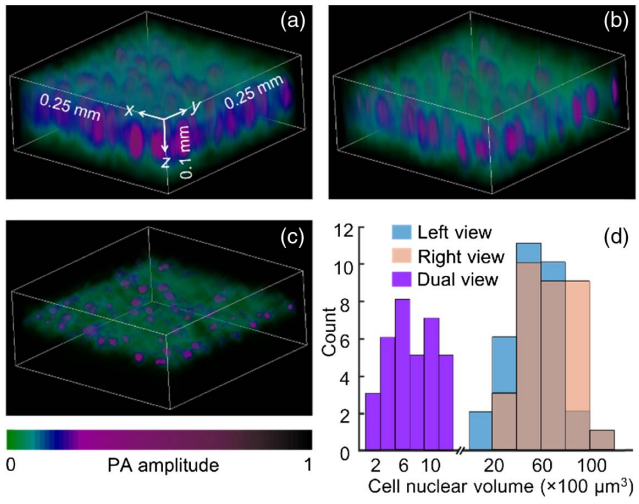

Fig. 5. Volumetric rendering of mouse brain slice images corresponding to the red dashed regions in Fig. 4 for (a) left view, (b) right view, and (c) dual view. (d) Histogram of the cell nuclear volumes imaged by the original two views and the dual view.

closer to the realistic cell nuclear volume if an average diameter of 6 μm and a spherical shape are assumed [23]. Cell nuclear volumes and shapes are important diagnostic features for cancer diagnosis [24].

In conclusion, a dual-view optical illumination for axial resolution improvement in OR-PAM was developed. Sub-resolution beads and carbon fiber phantoms were used to validate the axial resolution improvement and resolution isotropy. The SNR of the dual-view images was also improved. We used mouse brain slices to further demonstrate the efficacy of DV-OR-PAM for quantitative cell nuclear analysis. The DV-OR-PAM is a promising tool for cancer diagnosis by providing quantitative 3D cell nuclear information.

Funding. National Institutes of Health (NIH) (DP1 EB016986, R01 CA186567, U01 NS090579, U01 NS099717).

Acknowledgment. D. Cai appreciates the support from China Scholarship Council. L. V. Wang has a financial interest in Microphotoacoustics, Inc., CalPACT, LLC, and Union Photoacoustic Technologies, Ltd., which, however, did not support this work.

[†]These authors contributed equally to this work.

REFERENCES

1. L. V. Wang and J. Yao, Nat. Methods **13**, 627 (2016).
2. L. V. Wang and S. Hu, Science **335**, 1458 (2012).
3. C. Zhang, K. I. Maslov, S. Hu, L. V. Wang, R. Chen, Q. Zhou, and K. K. Shung, J. Biomed. Opt. **17**, 020501 (2012).
4. S. Hu, K. Maslov, and L. V. Wang, Opt. Lett. **36**, 1134 (2011).
5. T. T. Wong, R. Zhang, P. Hai, C. Zhang, M. A. Pleitez, R. L. Aft, D. V. Novack, and L. V. Wang, Sci. Adv. **3**, e1602168 (2017).
6. T. T. Wong, R. Zhang, C. Zhang, H.-C. Hsu, K. I. Maslov, L. Wang, J. Shi, R. Chen, K. K. Shung, and Q. Zhou, Nat. Commun. **8**, 1386 (2017).
7. D. Yao, R. Chen, K. Maslov, Q. Zhou, and L. V. Wang, J. Biomed. Opt. **17**, 056004 (2012).
8. D.-K. Yao, K. Maslov, K. K. Shung, Q. Zhou, and L. V. Wang, Opt. Lett. **35**, 4139 (2010).
9. E. M. Strohm, E. S. Berndl, and M. C. Kolios, Photoacoustics **1**, 49 (2013).
10. Z. Xie, S.-L. Chen, T. Ling, L. J. Guo, P. L. Carson, and X. Wang, Opt. Express **19**, 9027 (2011).
11. C. Zhang, K. I. Maslov, J. Yao, and L. V. Wang, J. Biomed. Opt. **17**, 116016 (2012).
12. Y. Yamaoka, M. Nambu, and T. Takamatsu, Opt. Express **19**, 13365 (2011).
13. X. Liu, T. T. Wong, J. Shi, J. Ma, Q. Yang, and L. V. Wang, Opt. Lett. **43**, 947 (2018).
14. L. Wang, C. Zhang, and L. V. Wang, Phys. Rev. Lett. **113**, 174301 (2014).
15. Y. Wu, P. Chandris, P. W. Winter, E. Y. Kim, V. Jaumouillé, A. Kumar, M. Guo, J. M. Leung, C. Smith, and I. Rey-Suarez, Optica **3**, 897 (2016).
16. S. Preibisch, F. Amat, E. Stamataki, M. Sarov, R. H. Singer, E. Myers, and P. Tomancak, Nat. Methods **11**, 645 (2014).
17. L. Zhu, L. Li, L. Gao, and L. V. Wang, Optica **1**, 217 (2014).
18. L. Zhu, L. Gao, L. Li, L. Wang, T. Ma, Q. Zhou, K. K. Shung, and L. V. Wang, Proc. SPIE **8943**, 89433H (2014).
19. Y. Wu, P. Wawrzusin, J. Senseney, R. S. Fischer, R. Christensen, A. Santella, A. G. York, P. W. Winter, C. M. Waterman, and Z. Bao, Nat. Biotechnol. **31**, 1032 (2013).
20. S. Preibisch, S. Saalfeld, J. Schindelin, and P. Tomancak, Nat. Methods **7**, 418 (2010).
21. V. Backman, M. B. Wallace, L. Perelman, J. Arendt, R. Gurjar, M. Müller, Q. Zhang, G. Zonios, E. Kline, and T. McGillican, Nature **406**, 35 (2000).
22. G. Vona, A. Sabile, M. Louha, V. Sitruk, S. Romana, K. Schütze, F. Capron, D. Franco, M. Pazzagli, and M. Vekemans, Am. J. Pathol. **156**, 57 (2000).
23. W. Bernhard and N. Granboulan, Exp. Cell Res. **9**, 19 (1963).
24. D. Zink, A. H. Fischer, and J. A. Nickerson, Nat. Rev. Cancer **4**, 677 (2004).